Research Square

Preprints are preliminary reports that have not undergone peer review.
They should not be considered conclusive, used to inform clinical practice,
or referenced by the media as validated information.

CFD assessment of non-premixed turbulent methane flame with reduced chemical kinetics

Mehul Bambhania

mehul.bambhania-med@msubaroda.ac.in

Maharaja Sayajirao University of Baroda

Dhruvkumar Jani

Maharaja Sayajirao University of Baroda

Jani Deepakkumar

Gyanmanjari Institute of Technology

Research Article

Keywords: Non-premixed combustion, Reduced chemical kinetics, RANS turbulence models, NO formation, Soot formation, Turbulence intensity

Posted Date: November 9th, 2026

DOI: https://doi.org/10.21203/rs.3.rs-11476477/v1

License: This work is licensed under a Creative Commons Attribution 4.0 International License.
Read Full License

Additional Declarations: No competing interests reported.

CFD assessment of non-premixed turbulent methane flame with reduced chemical kinetics

Mehul P. Bambhania[1,*], Jani Dhruvkumar Manishkumar[1], Jani Deepakkumar[2]

[1]Department of Mechanical Engineering, Faculty of Technology and Engineering, The Maharaja Sayajirao University of Baroda, Vadodara 390001, Gujarat, India

[2]Department of Mechanical Engineering

Gyanmanjari Institute of Technology, Bhavnagar, India.

[*]Corresponding author, e-mail: mehulbambhania-med@msubaroda.ac.in

ORCID: Mehul P. Bambhania 0000-0001-7910-5881

Received [Dates will be filled in by the Editorial office]

Abstract

Pollutant predictions in turbulent diffusion flames depend on how mixing, chemistry and their coupling are modelled. Using the Brookes–Moss experiments as reference, this study assesses how the Reynolds-averaged Navier–Stokes (RANS) turbulence closure, the chemical-kinetic scheme and the turbulence intensity of the air co-flow affect the computed structure, nitric oxide (NO) and soot of an enclosed methane jet flame at a Reynolds number of 5000. Steady axisymmetric simulations used the eddy-dissipation model, thermal and prompt NO post-processing and the Moss–Brookes soot model. The measured mixture fraction and the fast-chemistry limit were combined to bound the predicted fuel mass fraction. Of the closures tested (k–ε, k–ω and a Reynolds-stress model, RSM), the RSM lowered the mean absolute percentage error of the centreline temperature from 30.1% to 15.9%. Replacing the one-step scheme by a 16-step augmented reduced mechanism lowered the fuel-decay error from 56.6% to 9.5%, a larger gain than that obtained by changing the closure. Raising the co-flow turbulence intensity from 20% to 80% reduced the peak NO from 183 to 168 ppm (−8.4%) and the peak soot volume fraction by 43%. Centreline soot levels agreed with the measurements within 7%, although the radial soot extent was under-predicted.

Keywords: Non-premixed combustion; Reduced chemical kinetics; RANS turbulence models; NO formation; Soot formation; Turbulence intensity

Introduction

Natural gas, of which methane is the principal constituent, remains a major fuel for power generation, industrial furnaces and process heaters, and it is increasingly blended with hydrogen and biomethane in transitional low-carbon energy systems. Methane carries less carbon per hydrogen atom than any other hydrocarbon, yet its turbulent diffusion flames still release nitric oxide (NO) and soot; both are increasingly tightly regulated owing to their impact on air quality, health and the climate (Michelsen et al. 2020; Wang and Yang 2024). In confined burners, soot also controls flame radiation and therefore wall heat fluxes and the thermal efficiency of the equipment (Brookes and Moss 1999a; Valencia et al. 2021). For this reason, computational fluid dynamics (CFD) is now central to the development of low-emission burners, as long as turbulence, chemistry, pollutant formation and their interplay are modelled credibly (Eaton et al. 1999; Veynante and Vervisch 2002).

How well a Reynolds-averaged Navier–Stokes (RANS) computation of a diffusion flame performs depends primarily on its turbulence closure: fuel–air mixing fixes where the reaction zone sits, how long the flame is and how long the hot gases stay hot (Peters 2000; Poinsot and Veynante 2005). Industry still relies mostly on two-equation eddy-viscosity closures such as k–ε (Jones and Launder 1972; Launder and Spalding 1974) and k–ω (Wilcox 1988), although the standard k–ε variant spreads round jets too quickly, a defect known as the round-jet/plane-jet anomaly (Pope 1978). Reynolds stress models (RSM) (Launder et al. 1975; Gibson and Launder 1978) relax the isotropic eddy-viscosity assumption at a higher computational cost. For the piloted Sandia flame D, He et al. (2021) recently found that the RSM provided the closest agreement with measurements among five RANS closures, while da Silva et al. (2007, 2018) showed for a confined natural-gas flame that simple combustion models can rival more elaborate ones when the flow field is well predicted. Nanduri et al. (2010) reached a similar conclusion regarding emission predictions in a bluff-body combustor. Large-eddy simulation (LES) offers higher fidelity (Pitsch and Steiner 2000; Mueller and Pitsch 2012), but RANS remains the practical choice for parametric design studies.

The second ingredient is the chemical-kinetic description and its coupling with turbulence. In commercial RANS codes, turbulence–chemistry interaction (TCI) is often handled by the eddy-break-up (Spalding 1971) or eddy-dissipation (EDM) (Magnussen and Hjertager 1977) approaches, both of which let the turbulent mixing rate set the reaction rate. These models are inexpensive and robust, but they were formulated for one- or two-step global schemes (Westbrook and Dryer 1981; Jones and Lindstedt 1988) and cannot by themselves represent kinetically controlled processes; more elaborate closures such as the eddy-dissipation concept, flamelet or transported-PDF approaches are needed for those (Veynante and Vervisch 2002; Pope 2013; Bösenhofer et al. 2018). Comprehensive schemes like GRI-Mech 3.0 (53 species, 325 reversible steps) (Smith et al. 1999) are still costly in multi-dimensional turbulent computations, which is why systematic reduction methods have been developed (Lu and Law 2009). Reduced and augmented reduced mechanisms (ARM) derived from the GRI-Mech family retain the main pathways, including NO chemistry, with 12–17 lumped steps (Sung et al. 1998, 2001; TNF Workshop n.d.). The benefits of reduced chemistry were first demonstrated for laminar flames (Smooke et al. 1989; Schmidt et al. 1996; Yamashita et al. 1999; Yamashita 2000) and later in turbulent and practical configurations (Jazbec et al. 2000; Karalus et al. 2013; Guessab et al. 2014). Recent assessments (Zettervall et al. 2021; Wang et al. 2024) have shown that flame-structure and NOx predictions are highly sensitive to the mechanism, and that the amount of chemical detail needed is dictated by the quantity of interest and by the computing budget. Data-driven chemistry acceleration is an emerging alternative (Ihme et al. 2022).

The third ingredient is the representation of the pollutants themselves. Thermal NO is formed via the extended Zeldovich mechanism (Zeldovich 1946) and is strongly temperature dependent, whereas prompt NO is produced through hydrocarbon-radical attack on molecular nitrogen in the flame front (Fenimore 1971; De Soete 1975); comprehensive reviews of nitrogen chemistry are available (Miller and Bowman 1989; Glarborg et al. 2018). Soot evolves through inception, surface growth, coagulation and oxidation (Michelsen et al. 2020; Martin et al. 2022), and capturing its interaction with turbulence and radiation is still among the hardest tasks in combustion simulation (Raman and Fox 2016; Valencia et al. 2021). Semi-empirical two-equation soot models (Leung et al. 1991; Moss et al. 1995; Brookes and Moss 1999b) provide a pragmatic compromise and remain widely used in recent RANS studies of methane flames (Busupally and De 2016; Reddy et al. 2016; Garnayak et al. 2022; Rowhani et al. 2023; Uchoa Filho et al. 2025). Advanced approaches based on conditional

moment closure (Kronenburg et al. 2000; Woolley et al. 2009) or LES (Mueller and Pitsch 2012) improve accuracy at much higher cost.

The enclosed, atmospheric methane jet flame studied by Brookes and Moss (1999a) is a convenient benchmark: it offers mean profiles of temperature, mixture fraction and soot volume fraction, and it served to tune the popular Moss–Brookes soot model (Brookes and Moss 1999b). This and comparable enclosed flames have been used in pollutant studies; for example, Lopez-Parra and Turan (2007) perturbed the inflow and tracked the response of soot and NOx, and Saqr et al. (2010) found that a more turbulent free stream lowers both pollutants. However, the relative importance of the turbulence closure, of the fidelity of the chemical scheme and of the inlet turbulence level has rarely been quantified within a single, consistent numerical framework with explicit discretisation-error estimates and objective error metrics. In addition, the experimental database provides the mean mixture fraction rather than species concentrations, which complicates the validation of predicted fuel mass fractions and has not always been accounted for in earlier comparisons.

The present work addresses these gaps for the Brookes and Moss flame. Its specific contributions are: (i) a quantitative comparison of the standard k–ε, standard k–ω and RSM closures using centreline and radial error metrics; (ii) an assessment of one-step, two-step and 16-step reduced chemistry, in which the measured mixture fraction is used to construct physically consistent upper and lower bounds on the mean fuel mass fraction; (iii) a grid-convergence analysis based on the grid convergence index (GCI) (Roache 1994; Celik et al. 2008); and (iv) a parametric quantification of the effect of the air-stream turbulence intensity (20–80%) on the NO and soot fields. The reference experiment and the numerical approach are described in the Methods section, the results are discussed in the Results and discussion section, and the main findings are summarised in the Conclusions.

Methods

Reference experiment

Brookes and Moss (1999a) studied a piloted methane jet fired vertically upwards inside a Pyrex cylinder of 155 mm bore. The fuel (10.3 g min^{-1}) left a 4.07 mm nozzle at 20.3 m s^{-1} (exit Re = 5000) into a flow-straightened air stream of 708 g min^{-1}, both streams entering at 290 K and 1 atm. The flame was stabilised by a small fuel-rich premixed methane/oxygen pilot whose fuel flow was below 2% of the main fuel flow. Mean temperatures were obtained with fine-wire type-R thermocouples corrected for radiation

losses (corrections of up to about 50 K), the mean mixture fraction $\bar{\xi}$ from probe samples oxidised over a catalyst and analysed by mass spectrometry (minimum measurable value ≈ 0.02, uncertainty ≈ 6%), and the soot volume fraction f_v by tomographic laser extinction at 632.8 nm, for which the authors estimated an overall uncertainty of the order of 50% (Brookes and Moss 1999a). Centreline and radial profiles are available up to 425 mm above the burner exit, and soot profiles were reported from 300 mm downstream. Table 1 lists the conditions used in the computations.

Gas sampling yields the mixture fraction, the share of local mass that came from the fuel stream, rather than the concentration of unreacted methane. Since the methane mass fraction can never exceed the mixture fraction, $\bar{\xi}$ is an upper bound for $\tilde{Y}_{\mathrm{CH_4}}$. A lower bound follows from the fast-chemistry (Burke–Schumann) limit, in which methane and oxygen cannot coexist:

$$\tilde{Y}_{\mathrm{CH_4,min}} = \max\left(\frac{\bar{\xi}-\xi_{st}}{1-\xi_{st}},\, 0\right), \qquad \xi_{st} = \left(1+\frac{s\,Y_{\mathrm{F},1}}{Y_{\mathrm{O_2},2}}\right)^{-1} \tag{1}$$

where $s = 4$ is the oxygen mass required per unit mass of methane at stoichiometry, $Y_{\mathrm{F},1} = 1$ and $Y_{\mathrm{O_2},2} = 0.232$, giving $\xi_{st} = 0.055$. A physically consistent prediction of the mean methane mass fraction should therefore lie between the two bounds of Eq. (1), and this interval is used in the comparisons presented in the Results and discussion section. Strictly, Eq. (1) assumes equal diffusivities and applies to instantaneous values; it is used here as an engineering bound for the mean values, which is adequate because the centreline mixture fraction remains well above ξ_{st} throughout the measured region.

Table 1. Experimental and simulated operating and boundary conditions for the Brookes–Moss flame (Brookes and Moss 1999a).

Parameter	Fuel stream	Air stream
Composition (mass fractions)	CH_4 = 1.0	O_2 = 0.232, N_2 = 0.768
Mass flow rate/(kg s^{-1})	1.72×10^{-4} (10.3 g min^{-1})	1.18×10^{-2} (708 g min^{-1})
Inlet or hydraulic diameter/mm	4.07 (exp.); 4.0 (model)	155
Bulk velocity/(m s^{-1})	20.3	≈ 0.53
Reynolds number	5000	–

Parameter	Fuel stream	Air stream
Inlet temperature/K	290 (exp.); 300 (model)	290 (exp.); 300 (model)
Turbulence intensity/%	20	20 (baseline); 40, 80
Operating pressure	101.325 kPa	101.325 kPa
Global equivalence ratio	≈ 0.25	≈ 0.25
Outlet	Pressure outlet, 0 Pa gauge; backflow I = 10%, D_h = 159 mm	
Walls	Adiabatic, no-slip, standard wall functions	

Numerical methodology

Domain and boundary set-up

Because the burner and the confinement are axisymmetric and swirl-free, the flow was modelled as a steady, two-dimensional axisymmetric problem (Fig. 1). The domain spans 1.0 m axially from the nozzle and 77.5 mm radially; a 4 mm fuel inlet sits on the axis and the air inlet occupies the remaining annulus up to the wall. The pilot was not modelled, its mass flow being negligible compared with the main flows. Both streams enter through mass-flow inlets (Table 1); inflow turbulence is set by an intensity I and a hydraulic diameter D_h (4 mm for the fuel and 155 mm for the air). In the baseline case $I = 20\%$ was imposed on both streams. A pressure outlet (0 Pa gauge, backflow intensity 10%, D_h = 159 mm) was used at the exit, and the confining walls were treated as adiabatic, no-slip surfaces with standard wall functions. Radiation was not included in the energy equation; the consequences of this choice are discussed under Limitations and uncertainty.

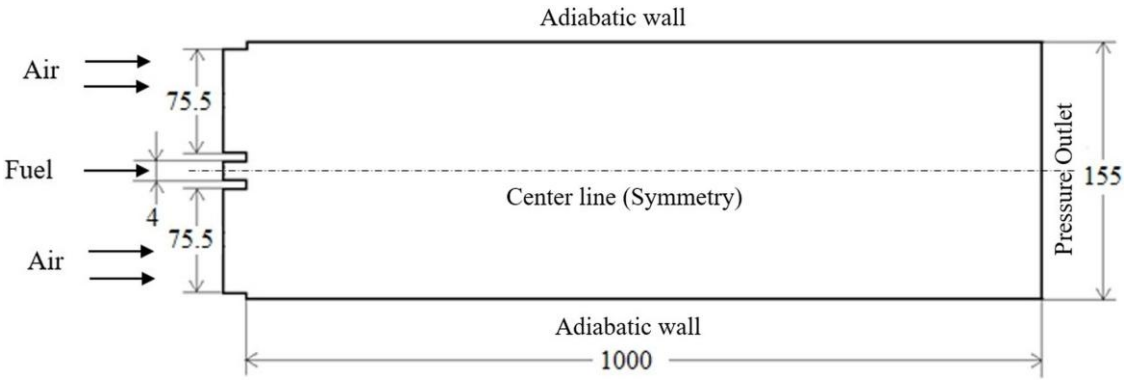


Fig. 1. Axisymmetric solution domain with its boundary types (mm).

The domain was discretised with a structured quadrilateral mesh generated in ANSYS ICEM CFD (Fig. 2). Cells were concentrated near the axis and the nozzle lip, where the jet/co-flow shear layer develops, and grown gradually in both directions; the lowest orthogonal quality was 0.999.

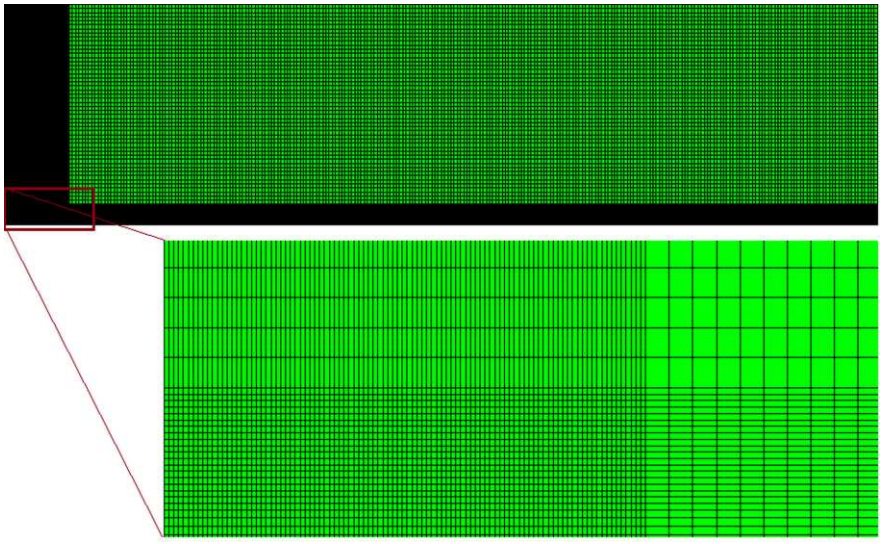


Fig. 2. Structured computational mesh with a detail of the refinement near the fuel nozzle.

Governing equations

The steady, density-weighted (Favre) balance equations solved here are:

$$\frac{\partial}{\partial x_j}\left(\bar{\rho}\,\tilde{u}_j\right) = 0 \tag{2}$$

$$\frac{\partial}{\partial x_j}\left(\bar{\rho}\,\tilde{u}_i\tilde{u}_j\right) = -\frac{\partial \bar{p}}{\partial x_i} + \frac{\partial}{\partial x_j}\left(\bar{\tau}_{ij} - \bar{\rho}\,\widetilde{u_i''u_j''}\right) \tag{3}$$

$$\frac{\partial}{\partial x_j}\left(\bar{\rho}\,\tilde{u}_j\tilde{h}\right) = \frac{\partial}{\partial x_j}\left[\left(\frac{\lambda}{c_p} + \frac{\mu_t}{Pr_t}\right)\frac{\partial \tilde{h}}{\partial x_j}\right] + \bar{S}_h \tag{4}$$

$$\frac{\partial}{\partial x_j}\left(\bar{\rho}\,\tilde{u}_j\tilde{Y}_k\right) = \frac{\partial}{\partial x_j}\left[\left(\bar{\rho}D_k + \frac{\mu_t}{Sc_t}\right)\frac{\partial \tilde{Y}_k}{\partial x_j}\right] + \bar{\omega}_k \tag{5}$$

where $\tilde{h}$ is the mixture enthalpy, $\tilde{Y}_k$ the mass fraction and $\bar{\omega}_k$ the mean chemical source of species k, μ_t the turbulent viscosity, and $Pr_t = 0.85$ and $Sc_t = 0.7$ the turbulent Prandtl and Schmidt numbers. Density follows from the ideal-gas equation of state for the mixture, and species heat capacities from piecewise polynomials.

Turbulence closures

In the eddy-viscosity models the turbulent stresses are linked to the mean strain via Boussinesq's assumption:

$$-\bar{\rho}\,\widetilde{u_i''u_j''} = \mu_t\left(\frac{\partial \tilde{u}_i}{\partial x_j} + \frac{\partial \tilde{u}_j}{\partial x_i}\right) - \frac{2}{3}\left(\bar{\rho}\,k + \mu_t\frac{\partial \tilde{u}_l}{\partial x_l}\right)\delta_{ij} \tag{6}$$

The standard k–ε model (Jones and Launder 1972; Launder and Spalding 1974) evaluates $\mu_t = \bar{\rho}\,C_\mu k^2/\varepsilon$ with the standard constants ($C_\mu = 0.09$, $C_{1\varepsilon} = 1.44$, $C_{2\varepsilon} = 1.92$, $\sigma_k = 1.0$, $\sigma_\varepsilon = 1.3$). The standard k–ω model (Wilcox 1988) evaluates $\mu_t = \bar{\rho}\,\alpha^* k/\omega$ and was used with the shear-flow (spreading-rate) correction and the production limiter activated. The RSM (Launder et al. 1975; Gibson and Launder 1978) instead carries a separate transport equation for each Reynolds-stress component $R_{ij} = \widetilde{u_i''u_j''}$,

$$\frac{\partial}{\partial x_k}\left(\bar{\rho}\,\tilde{u}_k R_{ij}\right) = P_{ij} + D_{ij} + \Phi_{ij} - \bar{\rho}\,\varepsilon_{ij} \tag{7}$$

where P_{ij}, D_{ij}, Φ_{ij} and ε_{ij} denote production, diffusion, pressure–strain and dissipation. The linear pressure–strain model ($C_1 = 1.8$, $C_2 = 0.6$, $C_1' = 0.5$) with wall-reflection effects was used, together with a transport equation for ε; in the present axisymmetric configuration this amounts to four Reynolds-stress equations plus the dissipation equation, compared with two equations for the eddy-viscosity models.

Turbulence–chemistry interaction

Mean reaction rates come from the Magnussen–Hjertager eddy-dissipation model (EDM) (Magnussen and Hjertager 1977), where each reaction r proceeds no faster than turbulence can mix either its reactants or the hot products,

$$\bar{R}_{k,r} = \nu'_{k,r} M_{w,k}\,A\,\bar{\rho}\,\frac{\varepsilon}{k}\,\min\left[\min_{\mathcal{R}}\left(\frac{\tilde{Y}_{\mathcal{R}}}{\nu'_{\mathcal{R},r}M_{w,\mathcal{R}}}\right),\; B\,\frac{\sum_{\mathcal{P}}\tilde{Y}_{\mathcal{P}}}{\sum_j \nu''_{j,r}M_{w,j}}\right] \tag{8}$$

with $A = 4.0$ and $B = 0.5$ (ANSYS Inc. 2019). Here ν' and ν'' denote the reactant- and product-side stoichiometric coefficients, M_w the molecular weights, and $\mathcal{R}$ and $\mathcal{P}$ denote reactants and products. The chemistry solver was set to relax the composition towards

chemical equilibrium with an aggressiveness factor of 0.5 (ANSYS Inc. 2019). Because the EDM is mixing-controlled, it is consistent with fast-chemistry assumptions; its use with multistep schemes is discussed under Influence of the chemical-kinetic scheme.

Chemical-kinetic schemes

Table 2 lists the three schemes in order of complexity: a single global step; the Westbrook–Dryer two-step scheme (Westbrook and Dryer 1981), which oxidises methane to CO and then CO to CO_2; and ARM2, a 16-step augmented reduced mechanism derived from GRI-Mech 2.11 (Bowman et al. n.d.) that retains NO chemistry and belongs to the ARM family of Sung et al. (1998, 2001). ARM2 is distributed by the TNF workshop (TNF Workshop n.d.) and was imported into the solver in CHEMKIN format (Kee et al. 1989).

Table 2. Chemical-kinetic schemes compared in this study.

Scheme	Global steps	Description	NO chemistry
One-step	1	$CH_4 + 2O_2 \rightarrow CO_2 + 2H_2O$	No
Two-step (Westbrook and Dryer 1981)	2	$CH_4 + 1.5O_2 \rightarrow CO + 2H_2O$; $CO + 0.5O_2 \rightleftharpoons CO_2$	No
ARM2 (Sung et al. 1998, 2001; TNF Workshop n.d.)	16	Augmented reduced mechanism derived from GRI-Mech 2.11 (Bowman et al. n.d.)	Yes

NO formation model

NO was obtained afterwards, on the converged flow solution, from a balance equation for the NO mass fraction,

$$\frac{\partial}{\partial x_j}\left(\bar{\rho}\,\tilde{u}_j \tilde{Y}_{\mathrm{NO}}\right) = \frac{\partial}{\partial x_j}\left(\bar{\rho}\,D_t \frac{\partial \tilde{Y}_{\mathrm{NO}}}{\partial x_j}\right) + \bar{S}_{\mathrm{NO}} \tag{9}$$

in which the source term contains the thermal and prompt contributions; fuel NO is absent for methane and the N_2O-intermediate route is significant mainly in lean, high-pressure, low-temperature combustion (Miller and Bowman 1989; Glarborg et al. 2018). For thermal NO, the extended Zeldovich scheme (Zeldovich 1946) was used:

$$\mathrm{O} + \mathrm{N_2} \rightleftharpoons \mathrm{N} + \mathrm{NO} \tag{10}$$

$$\mathrm{N} + \mathrm{O_2} \rightleftharpoons \mathrm{O} + \mathrm{NO} \tag{11}$$

$$\mathrm{N} + \mathrm{OH} \rightleftharpoons \mathrm{H} + \mathrm{NO} \tag{12}$$

Assuming the N atom to be in quasi-steady state yields the net thermal formation rate

$$\frac{\mathrm{d[NO]}}{\mathrm{d}t} = 2k_{f,1}[\mathrm{O}][\mathrm{N_2}]\,\frac{1-\frac{k_{r,1}k_{r,2}[\mathrm{NO}]^2}{k_{f,1}[\mathrm{N_2}]\,k_{f,2}[\mathrm{O_2}]}}{1+\frac{k_{r,1}[\mathrm{NO}]}{k_{f,2}[\mathrm{O_2}]+k_{f,3}[\mathrm{OH}]}} \tag{13}$$

where $k_{f,i}$ and $k_{r,i}$ denote the forward and backward rate constants of reactions (10)–(12), while the O and OH levels were taken from a partial-equilibrium assumption (ANSYS Inc. 2019). Owing to the high activation energy of the first reaction, the thermal route becomes significant only above about 1800 K. Prompt NO, initiated mainly by $\mathrm{CH} + \mathrm{N_2} \rightleftharpoons \mathrm{HCN} + \mathrm{N}$ (Fenimore 1971), was represented by the global rate of De Soete (1975) with the fuel-dependent correction factor implemented in the solver (ANSYS Inc. 2019). Turbulence–chemistry interaction for NO was accounted for by integrating the instantaneous source over an assumed β-function probability density function of temperature, $\bar{S}_{\mathrm{NO}} = \int_0^1 S_{\mathrm{NO}}(T)\,P(T)\,\mathrm{d}T$, with the temperature variance obtained from its own transport equation.

Soot model

Soot was modelled with the semi-empirical two-equation approach of Moss et al. (1995) and Brookes and Moss (1999b), which carries balance equations for the soot mass fraction Y_{soot} and the normalised radical-nuclei concentration $b^*_{nuc} = N/N_{norm}$ ($N_{norm} = 10^{15}$ particles):

$$\frac{\partial}{\partial x_j}\left(\bar{\rho}\,\tilde{u}_j Y_{soot}\right) = \frac{\partial}{\partial x_j}\left(\frac{\mu_t}{\sigma_{soot}}\frac{\partial Y_{soot}}{\partial x_j}\right) + \frac{\mathrm{d}M}{\mathrm{d}t} \tag{14}$$

$$\frac{\partial}{\partial x_j}\left(\bar{\rho}\,\tilde{u}_j b^*_{nuc}\right) = \frac{\partial}{\partial x_j}\left(\frac{\mu_t}{\sigma_{nuc}}\frac{\partial b^*_{nuc}}{\partial x_j}\right) + \frac{1}{N_{norm}}\frac{\mathrm{d}N}{\mathrm{d}t} \tag{15}$$

The particle-number source accounts for nucleation and coagulation, and the mass source for nucleation, surface growth and oxidation:

$$\frac{\mathrm{d}N}{\mathrm{d}t} = C_\alpha N_A \left(\frac{X_{prec}\,p}{RT}\right)^l e^{-T_\alpha/T} - C_\beta \left(\frac{24RT}{\rho_{soot}N_A}\right)^{1/2} d_p^{1/2} N^2 \tag{16}$$

$$\frac{\mathrm{d}M}{\mathrm{d}t} = \dot{\omega}_{nuc} + \dot{\omega}_{sg} - \dot{\omega}_{ox} \tag{17}$$

$$\dot{\omega}_{nuc} = M_P C_\alpha \left(\frac{X_{prec}\,p}{RT}\right)^l e^{-T_\alpha/T} \tag{18}$$

$$\dot{\omega}_{sg} = C_\gamma \left(\frac{X_{sgs}\,p}{RT}\right)^m e^{-T_\gamma/T}\left[(\pi N)^{1/3}\left(\frac{6M}{\rho_{soot}}\right)^{2/3}\right]^n \tag{19}$$

$$\dot{\omega}_{ox} = C_{oxid} C_\omega\,\eta_{coll}\left(\frac{X_{\mathrm{OH}}\,p}{RT}\right)\sqrt{T}\,(\pi N)^{1/3}\left(\frac{6M}{\rho_{soot}}\right)^{2/3} \tag{20}$$

where M denotes soot mass per unit volume, M_P the mass of a newly formed particle, X_{prec} and X_{sgs} give the mole fractions of the precursor and growth species (both taken as

methane), and the oxidation term $\dot{\omega}_{ox}$ describes oxidation by OH following Fenimore and Jones (1967). The model constants recommended for methane by Brookes and Moss (1999b) were used, and soot–turbulence interaction was accounted for through an assumed-PDF of temperature.

Solver settings and grid study

ANSYS Fluent 2019 R1 (academic licence) (ANSYS Inc. 2019) was used with its coupled pressure-based algorithm; convection was discretised with second-order upwinding, gradients with the least-squares cell-based method and pressure with second-order interpolation. A pseudo-transient under-relaxation strategy was used to aid convergence (Table 3). Convergence was accepted once every scaled residual had fallen by three or more decades and flattened, and the centreline monitors of temperature and NO had stopped changing.

Table 3. Numerical settings.

Item	Setting
Solver	Pressure-based, steady, coupled pressure–velocity scheme; 2D axisymmetric
Spatial discretisation	2nd-order upwind (momentum, turbulence, energy, species, NO, temperature variance); 2nd-order pressure; least-squares gradients
Pseudo-transient relaxation factors	p 0.5, velocity 0.5, ρ 0.25, k/ε/ω 0.75, species 0.75
Pseudo-transient time step	Automatic, aggressive length-scale method, time-scale factor 5
Turbulence–chemistry interaction	Eddy-dissipation model (A = 4, B = 0.5); relaxation to chemical equilibrium
NO model	Thermal (partial-equilibrium O/OH) and prompt (De Soete); β-PDF in temperature
Soot model	Moss–Brookes, methane constants; PDF in temperature
Near-wall treatment	Standard wall functions

Grid independence was examined with four meshes of 17,056, 32,117, 92,232 and 104,267 cells, using a monitored mean temperature as the target quantity (Fig. 3). Discretisation error was estimated by the three-mesh grid-convergence-index method of Celik

et al. (2008), using the representative cell size $h = (A/N)^{1/2}$ for the two-dimensional grids. With $h_1 < h_2 < h_3$ and $r_{21} = h_2/h_1$, the observed order p follows by fixed-point iteration of

$$p = \frac{1}{\ln r_{21}} \left| \ln \left| \frac{\varepsilon_{32}}{\varepsilon_{21}} \right| + \ln \left(\frac{r_{21}^{p} - s}{r_{32}^{p} - s} \right) \right|, \qquad s = \operatorname{sign}\left(\frac{\varepsilon_{32}}{\varepsilon_{21}} \right) \tag{21}$$

where $\varepsilon_{21} = \phi_2 - \phi_1$ and $\varepsilon_{32} = \phi_3 - \phi_2$. The fine-grid convergence index is then

$$GCI_{fine}^{21} = \frac{1.25\, e_a^{21}}{r_{21}^{p} - 1}, \qquad e_a^{21} = \left| \frac{\phi_1 - \phi_2}{\phi_1} \right| \tag{22}$$

The results are listed in Table 4. The observed order, p = 2.57, agrees with the formally second-order schemes, and the GCI on the finest grid is 0.49%. The temperature predicted on the 92,232-cell grid differs by only 0.35% from that on the 104,267-cell grid, which in turn lies within 0.05% of the Richardson-extrapolated value. All further runs therefore used the 92,232-cell mesh.

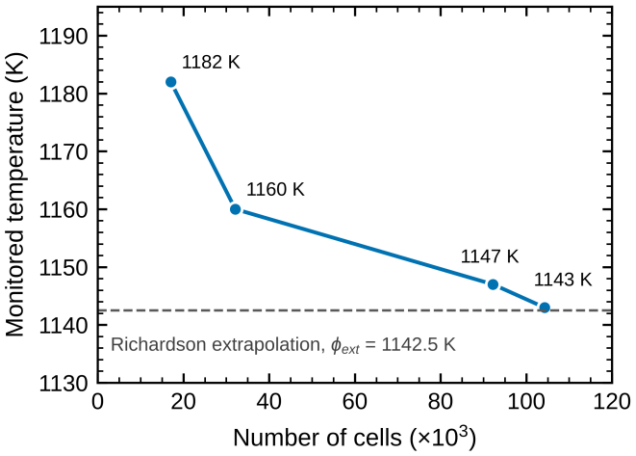


Fig. 3. Mesh study: monitored mean temperature versus cell count, with the Richardson-extrapolated limit.

Table 4. Grid convergence analysis following Celik et al. (2008) (φ = monitored mean temperature).

Quantity	**Value**
Number of cells N_1, N_2, N_3	92,232; 32,117; 17,056
r_{21}, r_{32}	1.695; 1.372
φ_1, φ_2, φ_3/K	1147; 1160; 1182
Apparent order p	2.57
Extrapolated value φ_{ext}^{21}/K	1142.5
Approximate relative error e_a^{21}/%	1.13

Quantity	Value
Extrapolated relative error e_{ext}^{21}/%	0.39
Fine-grid convergence index GCI_{fine}^{21}/%	0.49

Error metrics

For an objective comparison, three error measures (MAE, RMSE and MAPE: the absolute, quadratic and percentage mean deviations) were computed between predictions $\phi_{p,i}$ and measurements $\phi_{e,i}$ at the n measurement points:

$$\mathrm{MAE} = \frac{1}{n}\sum_{i=1}^{n}\left|\phi_{p,i} - \phi_{e,i}\right|, \qquad \mathrm{RMSE} = \sqrt{\frac{1}{n}\sum_{i=1}^{n}\left(\phi_{p,i} - \phi_{e,i}\right)^2} \tag{23}$$

$$\mathrm{MAPE} = \frac{100}{n}\sum_{i=1}^{n}\left|\frac{\phi_{p,i}-\phi_{e,i}}{\phi_{e,i}}\right| \tag{24}$$

Predictions were linearly interpolated to the measurement locations. For the methane mass fraction the MAPE is evaluated against $\bar{\xi}$, and the number of points lying inside the bounds of Eq. (1) is reported as an additional, physically based measure of consistency.

Results and discussion

Influence of the turbulence closure

Figure 4 compares the mean temperature fields predicted with the three turbulence closures using the one-step scheme. The closures produce visibly different flame shapes. The hot region is shortest and broadest with k–ε, as expected from its excessive round-jet spreading (Pope 1978); the RSM gives the longest, thinnest flame, hot almost to the outlet, and k–ω falls in between.

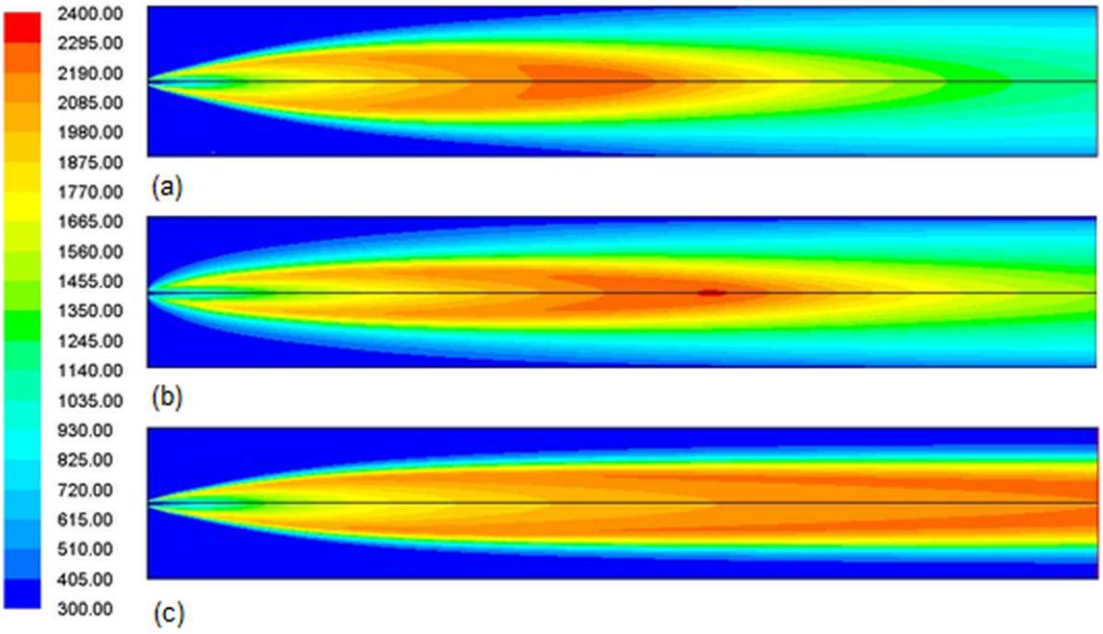


Fig. 4. Mean temperature (K) predicted with the one-step scheme and (a) standard k–ε, (b) standard k–ω and (c) RSM closures.

Fig. 5 quantifies these trends along the axis, and Table 5 gives the associated errors. All three closures over-predict the centreline temperature downstream of x ≈ 0.05 m. At x = 0.422 m the predicted values are 2216 K (k–ε), 2103 K (k–ω) and 1900 K (RSM), against a measured 1684 K, and the centreline MAPE decreases from 30.1% (k–ε) to 20.1% (k–ω) and 15.9% (RSM). The systematic over-prediction results from three modelling assumptions shared by all cases: (i) the walls are adiabatic and radiative losses, which are substantial in this sooting flame (Brookes and Moss 1999b; Reddy et al. 2016; Garnayak et al. 2022), are neglected; (ii) the one-step EDM converts the reactants directly into fully oxidised products, so that dissociation and the endothermic formation of CO and H_2 in the rich core are not represented; and (iii) the reactants enter at 300 K rather than 290 K, which accounts for only a small part of the difference. The same trends were reported for confined natural-gas flames by da Silva et al. (2007).

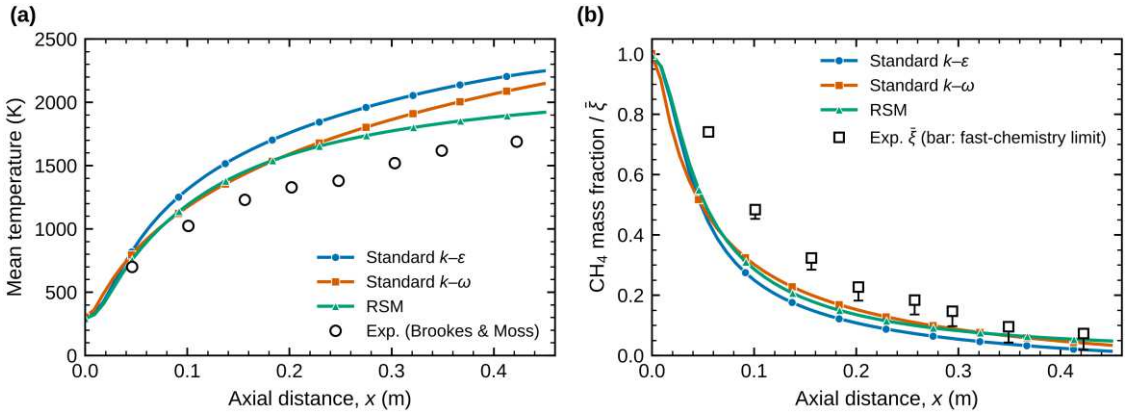


Fig. 5. Centreline profiles predicted with the one-step scheme and different turbulence closures: (a) mean temperature and (b) mean methane mass fraction. In (b), squares show the measured mean mixture fraction $\bar{\xi}$ (upper bound) and the bars extend to the fast-chemistry lower bound of Eq. (1). Experimental data from Brookes and Moss (1999a).

Along the axis (Fig. 5b), fuel disappears fastest with *k–ε*, whose curve falls below the lower bound of Eq. (1) at all stations (MAPE 56.6%), evidence of excessive jet mixing. The *k–ω* and RSM closures predict a slower decay that is in much closer agreement with the data (MAPE 37.9% and 38.6%, respectively), with two of the eight points inside the admissible interval in each case. The remaining discrepancy, a systematic under-prediction of the fuel concentration for x < 0.3 m, is attributable mainly to the one-step chemistry and is reduced substantially with multistep chemistry (see Influence of the chemical-kinetic scheme).

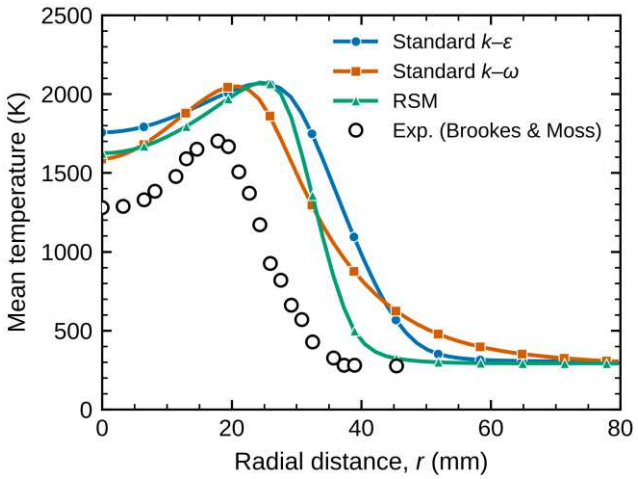


Fig. 6. Mean temperature versus radius at x = 0.2 m for the three closures (one-step chemistry).

Fig. 6 shows how temperature varies with radius at x = 0.2 m. The measured profile peaks off the axis, at 1703 K for r ≈ 17.8 mm, which locates the time-averaged reaction zone. All closures reproduce the off-axis peak, but locate it too far from the axis (r = 21.0–24.3 mm) and over-predict its magnitude (2048–2072 K). The width of the hot region is the most discriminating feature: the radius at which the temperature falls below 600 K is 43.7 mm for *k–ε*, 45.3 mm for *k–ω* and 37.3 mm for the RSM, compared with 29.2 mm in the experiment. The RSM thus captures the steep outer temperature gradient best, which is reflected in its lowest radial MAE (536 K) and MAPE (74.6%), although the *k–ω* closure gives a slightly lower RMSE (607 K versus 647 K) owing to its better centreline value.

Table 5. Error metrics of the turbulence closures (one-step scheme). Columns 2–4: centreline temperature; columns 5–6: centreline Y_{CH_4} compared with the measured mixture fraction, with the number of points satisfying the bounds of Eq. (1); columns 7–9 (Tr): radial temperature at x = 0.2 m.

Closure	**T MAE/ K**	**T RMSE/ K**	**T MAPE/ %**	**Y MAPE/ %**	**Y in bounds**	**Tr MAE/ K**	**Tr RMSE/ K**	**Tr MAPE/ %**
Standard k–ε	407	427	30.1	56.6	0/8	713	808	117.9
Standard k–ω	274	293	20.1	37.9	2/8	558	607	88.1
RSM	213	224	15.9	38.6	2/8	536	647	74.6

Overall, the RSM gave the best temperature predictions and the *k–ε* model the poorest, in agreement with recent assessments for Sandia flame D (He et al. 2021), whereas the *k–ω* and RSM closures performed comparably for the fuel decay. Because the *k–ω* closure achieved fuel-decay and radial-temperature accuracies comparable to those of the RSM while requiring only two turbulence transport equations instead of five, it was retained for the flame-structure and parametric analyses that follow, which involve a larger number of simulations.

Influence of the chemical-kinetic scheme

So that only the chemistry changes, all three schemes were run with the baseline *k–ε* closure; the one-step curve in Fig. 7 is thus the same as the *k–ε* curve in Fig. 5b. The

centreline methane decay depends strongly on the chemical description. The one-step scheme under-predicts the fuel concentration everywhere and lies outside the admissible interval at all stations (MAPE 56.6%). The two-step scheme of Westbrook and Dryer reduces the error to 28.8% and places three points within the bounds, and the 16-step ARM2 scheme reduces it further to 9.5%, with four points within the bounds and a mean distance from the admissible interval of only 0.022 (Table 6). The improvement obtained by refining the chemistry with the most diffusive closure therefore exceeds that obtained by changing the turbulence closure with one-step chemistry (Table 5), which underlines that in this flame the chemical description is at least as important as the turbulence model for the prediction of the fuel field.

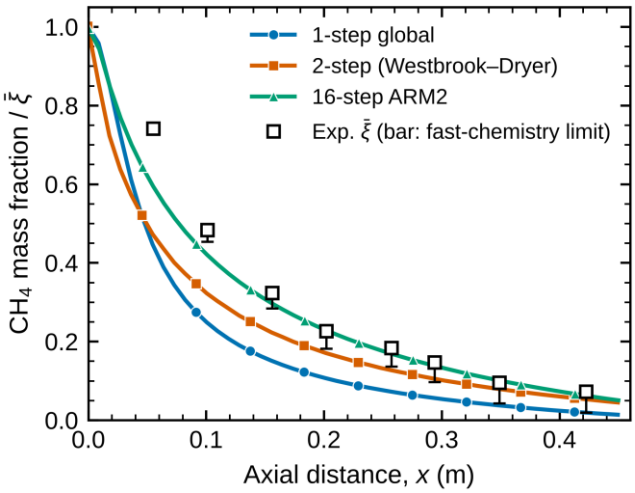


Fig. 7. Effect of the chemical-kinetic scheme on the centreline methane mass fraction (standard k–ε closure). Squares: measured $\bar{\xi}$; bars: fast-chemistry lower bound of Eq. (1).

Table 6. Effect of the chemical-kinetic scheme on the centreline methane mass fraction (standard k–ε closure).

Scheme	MAPE vs ξ/%	Points within bounds	Mean distance outside bounds	Y_{CH_4} at x = 0.2 m (bounds: 0.182–0.227)
One-step	56.6	0/8	0.101	0.106
Two-step	28.8	3/8	0.059	0.170
16-step ARM2	9.5	4/8	0.022	0.228

Fig. 8 compares the 16-step radial profiles with the data at x = 0.2, 0.3 and 0.425 m. The predicted profiles follow the measured shape closely: the MAPE with respect to $\bar{\xi}$ is

14.0%, 6.5% and 34.8% at the three stations, and 6 of 11, 5 of 11 and 7 of 7 measurement points, respectively, lie within the admissible interval. The larger percentage error at x = 0.425 m arises from the small absolute values near the edge of the jet (r > 15 mm), where the prediction lies below $\bar{\xi}$ but above the fast-chemistry bound, as expected physically in the vicinity of the reaction zone.

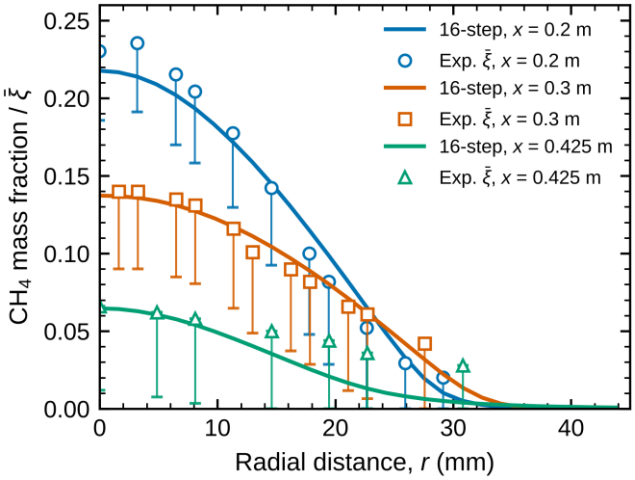


Fig. 8. Methane mass fraction versus radius at x = 0.2, 0.3 and 0.425 m, computed with ARM2 (16 steps). Symbols: measured $\bar{\xi}$; bars: fast-chemistry lower bound.

These improvements should be interpreted in the light of the TCI model. In the EDM framework every reaction step proceeds at the turbulent mixing rate limited by its scarcest reactant (Eq. (8)). In a reduced scheme, many lumped steps require radicals (H, O, OH) that are present only in small amounts, which throttles fuel consumption inside the rich core. This mimics, at least qualitatively, the finite-rate effects that delay fuel consumption in real flames, but it does not constitute a rigorous representation of kinetically controlled chemistry. The better agreement obtained with the multistep schemes is therefore encouraging but partly model dependent, and finite-rate TCI closures such as the eddy-dissipation concept or flamelet models (Veynante and Vervisch 2002; Bösenhofer et al. 2018) should be used to confirm it, particularly for minor species.

Flame structure

Figs. 9 and 10 present the time-averaged flame structure obtained with k–ω. Fuel occupies a narrow axial core that is used up within roughly half the chamber length (Fig. 9a), while hot gas reaches all the way to the exit (Fig. 9b), with a peak mean temperature of 2211 K. Such a structure is characteristic of a momentum-driven jet in a slow co-flow (≈ 0.53 m

s^{-1}): air is entrained gradually and the stoichiometric contour meets the axis far beyond the potential core.

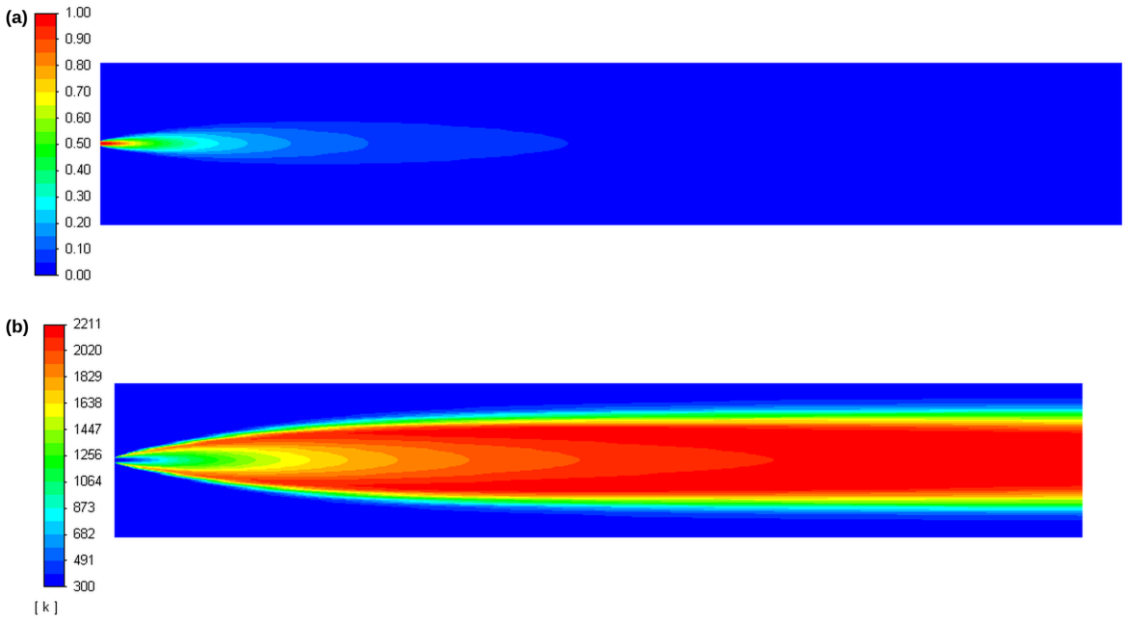


Fig. 9. Mean fields predicted with the standard k–ω closure: (a) methane mass fraction and (b) temperature (K).

Fig. 10 shows that the reaction zone is ring-shaped in cross-section. Off-axis maxima occur at x = 0.2 and 0.3 m, located at r ≈ 20.6–20.7 mm (2045 and 2121 K), while the centreline temperature rises from 1584 to 1857 K; at x = 0.425 m the maximum (2194 K) moves inward to r ≈ 16.3 mm and the centreline reaches 2103 K as the fuel core is consumed. The NO profiles closely follow the temperature: the NO maxima of 115.7, 146.1 and 166.4 ppm occur at r ≈ 20.4, 21.7 and 17.9 mm, i.e. practically at the locations of the temperature maxima. That NO peaks where temperature peaks, and keeps building up downstream, shows that the thermal pathway dominates here; its rate is set jointly by temperature and by how long the gas stays hot (Zeldovich 1946; Glarborg et al. 2018).

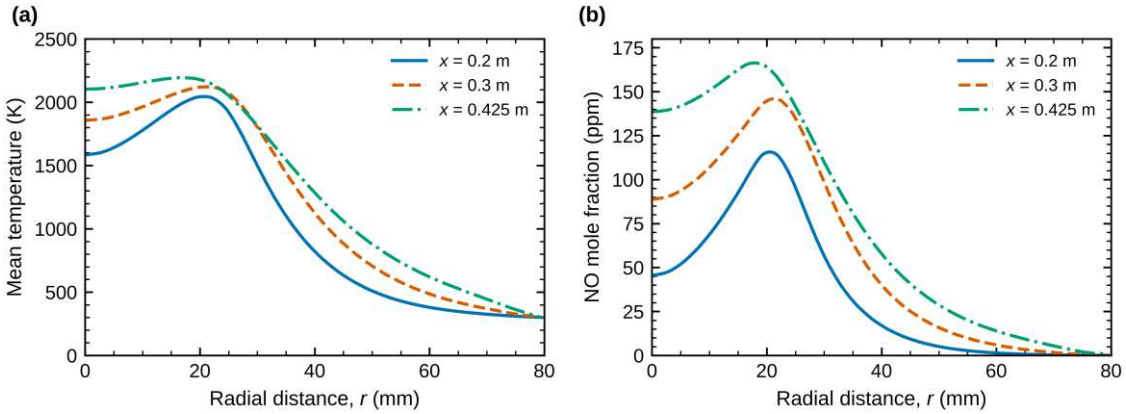


Fig. 10. Radial profiles at x = 0.2, 0.3 and 0.425 m (standard k–ω closure): (a) mean temperature and (b) NO mole fraction.

NO response to co-flow turbulence

The influence of the air-stream turbulence intensity I_{air} was examined for I_{air} = 20% (baseline), 40% and 80%, all other conditions being unchanged. The centreline NO distributions are shown in Fig. 11 and the NO fields for the two extreme cases in Fig. 12; the key quantities are summarised in Table 7. Upstream of x ≈ 0.4 m the three curves practically coincide, because the near field is dominated by the shear generated by the fuel jet itself. Further downstream, the higher co-flow turbulence lowers the NO level and shifts its maximum upstream: the peak centreline NO decreases from 183.0 ppm at x = 0.60 m (I_{air} = 20%) to 179.3 ppm at x = 0.58 m (40%) and 167.6 ppm at x = 0.55 m (80%), an 8.4% reduction. The effect is stronger downstream of the peak, where the outlet NO decreases from 72.9 to 58.0 ppm (−20.4%) and the axially averaged centreline NO from 99.0 to 87.3 ppm (−11.9%).

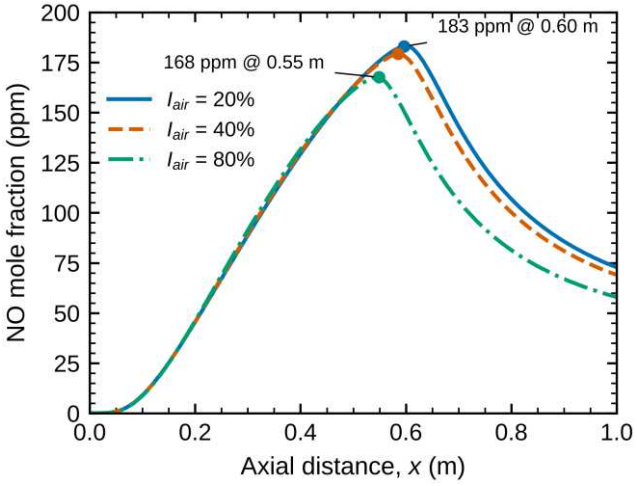


Fig. 11. Centreline NO mole fraction for air-stream turbulence intensities of 20%, 40% and 80%.

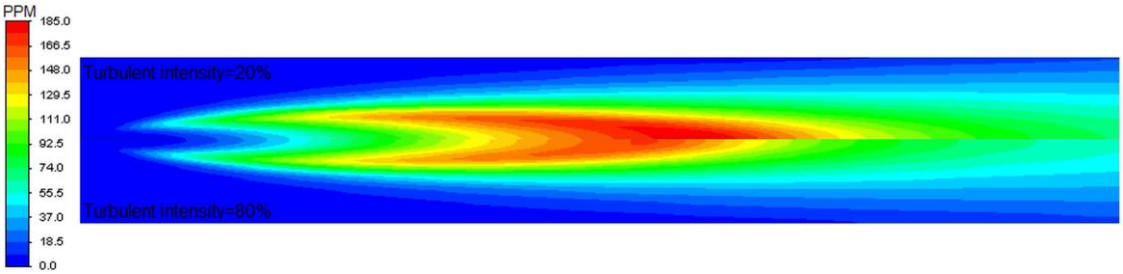


Fig. 12. NO mole fraction (ppm) for air-stream turbulence intensities of 20% (upper half) and 80% (lower half).

The reduction is consistent with the thermal character of NO formation identified in the analysis of the flame structure. Stronger co-flow turbulence raises the eddy diffusivity at the jet edge and speeds up the entrainment of cold air into the burnt gas. Burnout therefore occurs nearer the nozzle, as the upstream move of the NO maximum shows, and the products are diluted and cooled faster, so they spend less time in the hot zone where Zeldovich chemistry operates. Since the thermal NO rate grows exponentially with temperature and the amount formed scales with time, modest reductions in either produce a noticeable fall in NO. Similar reductions of NOx with increasing free-stream turbulence were reported by Saqr et al. (2010).

Table 7. Effect of the air-stream turbulence intensity on centreline NO and soot (standard k–ω closure).

Quantity	**I_{air} = 20%**	**I_{air} = 40%**	**I_{air} = 80%**	**Change, 20% → 80%**
Peak NO/ppm	183.0	179.3	167.6	−8.4%
Location of NO peak/m	0.60	0.58	0.55	−0.05 m
Outlet NO/ppm	72.9	69.1	58.0	−20.4%
Axially averaged NO/ppm	99.0	96.3	87.3	−11.9%
Peak soot volume fraction ($\times 10^{-7}$)	3.73	–	2.13	−42.9%
Location of soot peak/m	0.37	–	0.33	−0.04 m
Sooting region, $f_v > 10^{-8}$/m	0.19–0.46	–	0.19–0.41	−18%
Integrated centreline f_v ($\times 10^{-8}$ m)	4.88	–	2.44	−50.0%

Soot formation

Fig. 13 sets the computed radial soot profiles against the data. The magnitude of the soot volume fraction on the axis is captured well: the predicted values are 7.0×10^{-8} at x = 0.3 m and 1.64×10^{-7} at x = 0.425 m, compared with measured values of 6.6×10^{-8} and 1.63×10^{-7}, i.e. within 7%, which is far smaller than the experimental uncertainty. The predicted increase of soot with height between the two stations is also reproduced. The soot zone is, however, too narrow: its computed half-width at half maximum is 14.2 mm (x = 0.3 m) and 12.7 mm (x = 0.425 m), against measured values of 24.8 and 33.2 mm. The narrower predicted soot zone may be attributed to the neglect of radiation and thermophoresis, to the absence of soot transport effects specific to particles (differential diffusion) (Woolley et al. 2009), to the use of methane as the soot precursor rather than acetylene or aromatic species (Busupally and De 2016; Reddy et al. 2016), and to the treatment of OH oxidation at the flame edge, to which soot predictions are known to be very sensitive (Reddy et al. 2016). Similar under-predictions of the soot spread were reported with semi-empirical models in RANS simulations of methane flames (Brookes and Moss 1999b; Kronenburg et al. 2000).

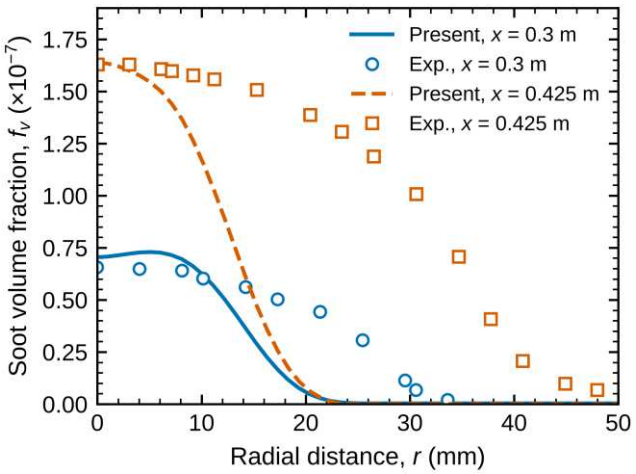


Fig. 13. Soot volume fraction versus radius at x = 0.3 and 0.425 m. Experimental data from Brookes and Moss (1999a).

Soot responds strongly to the co-flow turbulence level (Figs. 14 and 15). Increasing I_{air} from 20% to 80% decreases the peak centreline soot volume fraction from 3.73×10^{-7} to 2.13×10^{-7} (−43%), moves the peak upstream from x = 0.37 to 0.33 m and shortens the sooting region (where $f_v > 10^{-8}$) from 0.19–0.46 m to 0.19–0.41 m. Integrated along the axis, a proxy for the total soot loading, the soot volume fraction drops by half. The contours in Fig.

15 confirm that the soot-containing region shrinks in both length and width. Soot inception and surface growth require fuel-rich gases at high temperature; the enhanced mixing produced by the more turbulent co-flow reduces the residence time of the gases in this fuel-rich, high-temperature region and accelerates the supply of oxidising species, both of which limit soot growth and promote its oxidation. The trend agrees with the decrease of soot with increasing free-stream turbulence reported by Saqr et al. (2010) and with the sensitivity of soot emissions to inflow conditions observed by Lopez-Parra and Turan (2007).

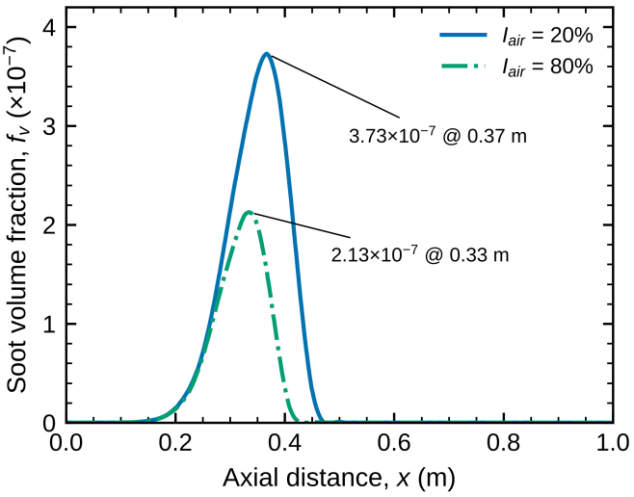


Fig. 14. Centreline soot volume fraction for air-stream turbulence intensities of 20% and 80%.

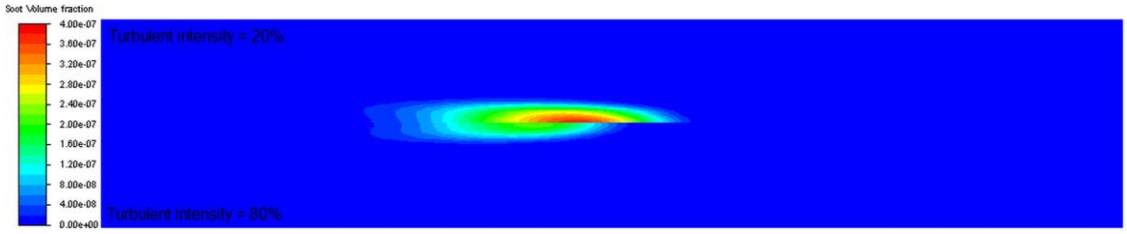


Fig. 15. Soot volume fraction for air-stream turbulence intensities of 20% (upper half) and 80% (lower half).

Taken together, the NO and soot results show that the co-flow turbulence intensity affects soot much more strongly than NO: a fourfold increase in I_{air} reduces the peak NO by 8% but the peak soot by 43%. The contrast stems from what each pollutant responds to: soot is governed by how large and long-lived the hot, fuel-rich zone is, a property controlled by mixing, whereas NO follows mainly the peak temperature, which changes only moderately. Enhancing co-flow turbulence thus appears to be an effective means of reducing soot without a NO penalty in confined diffusion flames, as it reduces both.

Limitations and uncertainty

Several limitations of the present approach must be considered when interpreting the results. First, the walls were treated as adiabatic and radiation was not modelled; this is the main cause of the centreline temperature over-prediction, which reaches about 530 K with the standard k–ε closure and 310 K with the RSM. Because thermal NO depends exponentially on temperature, the absolute NO levels are likely to be over-estimated, and the relative trends (Table 7) are more reliable than the absolute values. Second, the EDM is a mixing-controlled closure; its combination with multistep chemistry is pragmatic rather than rigorous (see Influence of the chemical-kinetic scheme), and finite-rate closures should be used to predict minor species and CO. Third, the measured mixture fraction was used to construct bounds on the fuel mass fraction rather than as a direct measure of it; direct comparisons of the predicted mixture fraction would further strengthen the validation. Fourth, the simulations are steady and two-dimensional, and inflow turbulence was specified through intensity and length-scale boundary conditions; the 20–80% range of turbulence intensity is higher than would be expected for the straightened co-flow of the experiment and was chosen deliberately to bracket the sensitivity of the pollutants. Finally, the semi-empirical soot model uses methane-specific constants; coupling it with radiation (for example, a discrete-ordinates solver with grey-gas-mixture absorption coefficients) and with better precursor chemistry should improve the predicted soot spread (Valencia et al. 2021; Garnayak et al. 2022). These aspects define natural extensions of the present work, together with LES of the same configuration.

Conclusions

RANS simulations of the Brookes–Moss enclosed methane jet flame were used to quantify how the turbulence closure, the kinetic scheme and the co-flow turbulence intensity affect the computed flame structure, NO and soot. The main conclusions are as follows.

1. With an observed order of 2.57 and a fine-grid GCI of 0.49%, the discretisation error is negligible relative to the modelling error.
2. All closures over-predicted the centreline temperature, mainly because of the adiabatic, non-radiating treatment and the one-step chemistry. The RSM reduced the centreline temperature MAPE from 30.1% (standard k–ε) to 15.9% and best reproduced the radial width of the hot region, whereas the k–ω and RSM closures predicted the fuel decay with comparable accuracy (MAPE $\approx$ 38%).

3. Using the measured mixture fraction and the fast-chemistry limit to bound the mean fuel mass fraction provided a physically consistent validation criterion. Replacing the one-step scheme with the 16-step ARM2 mechanism reduced the centreline fuel-decay error from 56.6% to 9.5%, which exceeds the improvement obtained by changing the turbulence closure.
4. NO formation was dominated by the thermal route: the NO maxima coincided with the off-axis temperature maxima at r ≈ 18–22 mm and NO accumulated downstream.
5. Increasing the air-stream turbulence intensity from 20% to 80% reduced the peak centreline NO from 183 to 168 ppm (−8.4%), moved it 0.05 m upstream and reduced the outlet NO by 20%.
6. The centreline soot levels were predicted within 7% of the measurements at x = 0.3 and 0.425 m, but the radial extent of the soot region was under-predicted by a factor of about two. Going from 20% to 80% intensity lowered the peak soot by 43% and the axially integrated soot by 50%.

These results indicate that, for low-cost engineering predictions of pollutants in confined diffusion flames, a closure that avoids the round-jet spreading error of the standard k–ε model should be combined with at least a reduced multistep mechanism, and that co-flow turbulence can be used as an effective means of reducing soot without increasing NO. Future work will include radiation, finite-rate turbulence–chemistry interaction and large-eddy simulation of the same configuration.

Symbols

A, B	constants of the eddy-dissipation model	
b^*_{nuc}	normalised radical-nuclei concentration	
D_{h}	hydraulic diameter	m
f_{v}	soot volume fraction	
h	enthalpy per unit mass; characteristic grid spacing	J kg^{-1}; m
I	turbulence intensity	%
k	turbulence kinetic energy	m^2 s^{-2}
M	soot mass per unit volume	kg m^{-3}
N	soot particle number per unit volume	m^{-3}
p	pressure; observed order of convergence	Pa; –
Pr_{t}	turbulent Prandtl number	

r	radius; ratio of grid spacings	m; –
R_{ij}	Reynolds stress tensor	$m^2\ s^{-2}$
Sc_t	turbulent Schmidt number	
T	temperature	K
u_i	velocity component	$m\ s^{-1}$
x	axial distance from the nozzle	m
Y_k	mass fraction of species k	

Greek letters

ε	turbulence dissipation rate	$m^2\ s^{-3}$
μ_t	turbulent viscosity	Pa s
ξ	mixture fraction	
ξ_{st}	stoichiometric mixture fraction	
ρ	density	$kg\ m^{-3}$
ω	specific dissipation rate	s^{-1}

Abbreviations

ARM2	16-step augmented reduced mechanism
EDM	eddy-dissipation model
GCI	grid convergence index
MAE	mean absolute error
MAPE	mean absolute percentage error
RANS	Reynolds-averaged Navier–Stokes
RMSE	root-mean-square error
RSM	Reynolds stress model
TCI	turbulence–chemistry interaction

Statements and declarations

Funding The authors did not receive support from any organization for the submitted work.

Competing interests Authors have no competing interests to declare that are relevant to the content of this article.

Author contributions Mehul P. Bambhania: Conceptualization, Methodology, Investigation, Formal analysis, Writing – original draft, Jani Dhruvkumar Manishkumar: Writing – formatting & editing draft and images. Jani Deepakkumar: Review & Editing.

Data availability Data will be made available on request.

References

ANSYS Inc. (2019) ANSYS Fluent theory guide, release 2019 R1. ANSYS Inc., Canonsburg, PA

Bösenhofer M, Wartha E-M, Jordan C, Harasek M (2018) The eddy dissipation concept—analysis of different fine structure treatments for classical combustion. Energies 11:1902. https://doi.org/10.3390/en11071902

Bowman CT, Hanson RK, Davidson DF, Gardiner WC Jr, Lissianski V, Smith GP, Golden DM, Frenklach M, Goldenberg M (n.d.) GRI-Mech 2.11. http://combustion.berkeley.edu/gri-mech/. Accessed 15 October 2026

Brookes SJ, Moss JB (1999a) Measurements of soot production and thermal radiation from confined turbulent jet diffusion flames of methane. Combust Flame 116:49–61. https://doi.org/10.1016/S0010-2180(98)00027-3

Brookes SJ, Moss JB (1999b) Predictions of soot and thermal radiation properties in confined turbulent jet diffusion flames. Combust Flame 116:486–503. https://doi.org/10.1016/S0010-2180(98)00056-X

Busupally MR, De A (2016) Numerical modeling of soot formation in a turbulent C_2H_4/air diffusion flame. Int J Spray Combust Dyn 8:67–85. https://doi.org/10.1177/1756827716638814

Celik IB, Ghia U, Roache PJ, Freitas CJ, Coleman H, Raad PE (2008) Procedure for estimation and reporting of uncertainty due to discretization in CFD applications. J Fluids Eng 130:078001. https://doi.org/10.1115/1.2960953

da Silva CV, França FHR, Vielmo HA (2007) Analysis of the turbulent, non-premixed combustion of natural gas in a cylindrical chamber with and without thermal radiation. Combust Sci Technol 179:1605–1630. https://doi.org/10.1080/00102200701244710

da Silva CV, Deon DL, Centeno FR, França FHR, Pereira FM (2018) Assessment of combustion models for numerical simulations of a turbulent non-premixed natural gas

flame inside a cylindrical chamber. Combust Sci Technol 190:1528–1556. https://doi.org/10.1080/00102202.2018.1456430

De Soete GG (1975) Overall reaction rates of NO and N_2 formation from fuel nitrogen. Symp (Int) Combust 15:1093–1102. https://doi.org/10.1016/S0082-0784(75)80374-2

Eaton AM, Smoot LD, Hill SC, Eatough CN (1999) Components, formulations, solutions, evaluation, and application of comprehensive combustion models. Prog Energy Combust Sci 25:387–436. https://doi.org/10.1016/S0360-1285(99)00008-8

Fenimore CP (1971) Formation of nitric oxide in premixed hydrocarbon flames. Symp (Int) Combust 13:373–380. https://doi.org/10.1016/S0082-0784(71)80040-1

Fenimore CP, Jones GW (1967) Oxidation of soot by hydroxyl radicals. J Phys Chem 71:593–597. https://doi.org/10.1021/j100862a021

Garnayak S, Pasha AA, Alsulami R, Nemitallah MA, Abdul Jameel AG, Dash SK, Reddy VM (2022) Numerical investigation to evaluate the effects of gravity and pressure on flame structure and soot formation of turbulent non-premixed methane–air flame. Propuls Power Res 11:473–495. https://doi.org/10.1016/j.jppr.2022.09.004

Gibson MM, Launder BE (1978) Ground effects on pressure fluctuations in the atmospheric boundary layer. J Fluid Mech 86:491–511. https://doi.org/10.1017/S0022112078001251

Glarborg P, Miller JA, Ruscic B, Klippenstein SJ (2018) Modeling nitrogen chemistry in combustion. Prog Energy Combust Sci 67:31–68. https://doi.org/10.1016/j.pecs.2018.01.002

Guessab A, Aris A, Bounif A, Gökalp I (2014) Reduced chemical kinetic mechanisms: simulation of turbulent non-premixed CH_4–air flame. Jordan J Mech Ind Eng 8:66–74

He D, Yu Y, Kuang Y, Wang C (2021) Model comparisons of flow and chemical kinetic mechanisms for methane–air combustion for engineering applications. Appl Sci 11:4107. https://doi.org/10.3390/app11094107

Ihme M, Chung WT, Mishra AA (2022) Combustion machine learning: principles, progress and prospects. Prog Energy Combust Sci 91:101010. https://doi.org/10.1016/j.pecs.2022.101010

Jazbec M, Fletcher DF, Haynes BS (2000) Simulation of the ignition of lean methane mixtures using CFD modelling and a reduced chemistry mechanism. Appl Math Model 24:689–696. https://doi.org/10.1016/S0307-904X(00)00012-3

Jones WP, Launder BE (1972) The prediction of laminarization with a two-equation model of turbulence. Int J Heat Mass Transf 15:301–314. https://doi.org/10.1016/0017-9310(72)90076-2

Jones WP, Lindstedt RP (1988) Global reaction schemes for hydrocarbon combustion. Combust Flame 73:233–249. https://doi.org/10.1016/0010-2180(88)90021-1

Karalus MF, Fackler KB, Novosselov IV, Kramlich JC, Malte PC (2013) A skeletal mechanism for the reactive flow simulation of methane combustion. In: Proceedings of ASME Turbo Expo 2013: Turbine Technical Conference and Exposition, vol 1B: Combustion, Fuels and Emissions. ASME, San Antonio, Paper GT2013-95904, V01BT04A065. https://doi.org/10.1115/GT2013-95904

Kee RJ, Rupley FM, Miller JA (1989) Chemkin-II: a Fortran chemical kinetics package for the analysis of gas-phase chemical kinetics. Sandia Report SAND89-8009. Sandia National Laboratories, Livermore, CA. https://doi.org/10.2172/5681118

Kronenburg A, Bilger RW, Kent JH (2000) Modeling soot formation in turbulent methane–air jet diffusion flames. Combust Flame 121:24–40. https://doi.org/10.1016/S0010-2180(99)00146-7

Launder BE, Spalding DB (1974) The numerical computation of turbulent flows. Comput Methods Appl Mech Eng 3:269–289. https://doi.org/10.1016/0045-7825(74)90029-2

Launder BE, Reece GJ, Rodi W (1975) Progress in the development of a Reynolds-stress turbulence closure. J Fluid Mech 68:537–566. https://doi.org/10.1017/S0022112075001814

Leung KM, Lindstedt RP, Jones WP (1991) A simplified reaction mechanism for soot formation in nonpremixed flames. Combust Flame 87:289–305. https://doi.org/10.1016/0010-2180(91)90114-Q

Lopez-Parra F, Turan A (2007) Computational study on the effects of non-periodic flow perturbations on the emissions of soot and NOx in a confined turbulent methane/air diffusion flame. Combust Sci Technol 179:1361–1384. https://doi.org/10.1080/00102200601147898

Lu T, Law CK (2009) Toward accommodating realistic fuel chemistry in large-scale computations. Prog Energy Combust Sci 35:192–215. https://doi.org/10.1016/j.pecs.2008.10.002

Magnussen BF, Hjertager BH (1977) On mathematical modeling of turbulent combustion with special emphasis on soot formation and combustion. Symp (Int) Combust 16:719–729. https://doi.org/10.1016/S0082-0784(77)80366-4

Martin JW, Salamanca M, Kraft M (2022) Soot inception: carbonaceous nanoparticle formation in flames. Prog Energy Combust Sci 88:100956. https://doi.org/10.1016/j.pecs.2021.100956

Michelsen HA, Colket MB, Bengtsson P-E, D'Anna A, Desgroux P, Haynes BS, Miller JH, Nathan GJ, Pitsch H, Wang H (2020) A review of terminology used to describe soot formation and evolution under combustion and pyrolytic conditions. ACS Nano 14:12470–12490. https://doi.org/10.1021/acsnano.0c06226

Miller JA, Bowman CT (1989) Mechanism and modeling of nitrogen chemistry in combustion. Prog Energy Combust Sci 15:287–338. https://doi.org/10.1016/0360-1285(89)90017-8

Moss JB, Stewart CD, Young KJ (1995) Modeling soot formation and burnout in a high temperature laminar diffusion flame burning under oxygen-enriched conditions. Combust Flame 101:491–500. https://doi.org/10.1016/0010-2180(94)00233-I

Mueller ME, Pitsch H (2012) LES model for sooting turbulent nonpremixed flames. Combust Flame 159:2166–2180. https://doi.org/10.1016/j.combustflame.2012.02.001

Nanduri JR, Parsons DR, Yilmaz SL, Celik IB, Strakey PA (2010) Assessment of RANS-based turbulent combustion models for prediction of emissions from lean premixed combustion of methane. Combust Sci Technol 182:794–821. https://doi.org/10.1080/00102200903341546

Peters N (2000) Turbulent combustion. Cambridge University Press, Cambridge. https://doi.org/10.1017/CBO9780511612701

Pitsch H, Steiner H (2000) Large-eddy simulation of a turbulent piloted methane/air diffusion flame (Sandia flame D). Phys Fluids 12:2541–2554. https://doi.org/10.1063/1.1288493

Poinsot T, Veynante D (2005) Theoretical and numerical combustion, 2nd edn. R.T. Edwards, Philadelphia

Pope SB (1978) An explanation of the turbulent round-jet/plane-jet anomaly. AIAA J 16:279–281. https://doi.org/10.2514/3.7521

Pope SB (2013) Small scales, many species and the manifold challenges of turbulent combustion. Proc Combust Inst 34:1–31. https://doi.org/10.1016/j.proci.2012.09.009

Raman V, Fox RO (2016) Modeling of fine-particle formation in turbulent flames. Annu Rev Fluid Mech 48:159–190. https://doi.org/10.1146/annurev-fluid-122414-034306

Reddy BM, De A, Yadav R (2016) Numerical investigation of soot formation in turbulent diffusion flame with strong turbulence–chemistry interaction. J Therm Sci Eng Appl 8:011001. https://doi.org/10.1115/1.4030694

Roache PJ (1994) Perspective: a method for uniform reporting of grid refinement studies. J Fluids Eng 116:405–413. https://doi.org/10.1115/1.2910291

Rowhani A, Sun Z, Chinnici A, Medwell PR, Nathan GJ, Dally BB (2023) Soot structure and flow characteristics in turbulent non-premixed methane flames stabilised on a bluff-body. Fuel 344:128118. https://doi.org/10.1016/j.fuel.2023.128118

Saqr KM, Aly HS, Sies MM, Wahid MA (2010) Effect of free stream turbulence on NOx and soot formation in turbulent diffusion CH_4–air flames. Int Commun Heat Mass Transf 37:611–617. https://doi.org/10.1016/j.icheatmasstransfer.2010.02.008

Schmidt D, Segatz J, Riedel U, Warnatz J, Maas U (1996) Simulation of laminar methane–air flames using automatically simplified chemical kinetics. Combust Sci Technol 113:3–16. https://doi.org/10.1080/00102209608935484

Smith GP, Golden DM, Frenklach M, Moriarty NW, Eiteneer B, Goldenberg M, Bowman CT, Hanson RK, Song S, Gardiner WC Jr, Lissianski VV, Qin Z (1999) GRI-Mech 3.0. http://combustion.berkeley.edu/gri-mech/. Accessed 15 October 2026

Smooke MD, Mitchell RE, Keyes DE (1989) Numerical solution of two-dimensional axisymmetric laminar diffusion flames. Combust Sci Technol 67:85–122. https://doi.org/10.1080/00102208908924063

Spalding DB (1971) Mixing and chemical reaction in steady confined turbulent flames. Symp (Int) Combust 13:649–657. https://doi.org/10.1016/S0082-0784(71)80067-X

Sung CJ, Law CK, Chen J-Y (1998) An augmented reduced mechanism for methane oxidation with comprehensive global parametric validation. Symp (Int) Combust 27:295–304. https://doi.org/10.1016/S0082-0784(98)80416-5

Sung CJ, Law CK, Chen J-Y (2001) Augmented reduced mechanisms for NO emission in methane oxidation. Combust Flame 125:906–919. https://doi.org/10.1016/S0010-2180(00)00248-0

TNF Workshop (n.d.) Chemical mechanisms. International Workshop on Measurement and Computation of Turbulent Nonpremixed Flames, Sandia National Laboratories. https://www.sandia.gov/TNF/chemistry.html. Accessed 15 October 2026

Uchoa Filho FEL, Sampaio HCM, Moura Júnior CFF, de Oliveira MLM, Thé JVG, Rocha PAC, Bueno AV (2025) Radiation and combustion effects of hydrogen enrichment on biomethane flames. Processes 13:1048. https://doi.org/10.3390/pr13041048

Valencia S, Ruiz S, Manrique J, Celis C, Figueira da Silva LF (2021) Soot modeling in turbulent diffusion flames: review and prospects. J Braz Soc Mech Sci Eng 43:219. https://doi.org/10.1007/s40430-021-02876-y

Veynante D, Vervisch L (2002) Turbulent combustion modeling. Prog Energy Combust Sci 28:193–266. https://doi.org/10.1016/S0360-1285(01)00017-X

Wang Z, Yang X (2024) NOx formation mechanism and emission prediction in turbulent combustion: a review. Appl Sci 14:6104. https://doi.org/10.3390/app14146104

Wang Y, Han HS, Sohn CH (2024) A comparative study of chemical-kinetic mechanisms for combustion of methane/hydrogen/air mixtures. Int J Aeronaut Space Sci 25:519–539. https://doi.org/10.1007/s42405-023-00671-8

Westbrook CK, Dryer FL (1981) Simplified reaction mechanisms for the oxidation of hydrocarbon fuels in flames. Combust Sci Technol 27:31–43. https://doi.org/10.1080/00102208108946970

Wilcox DC (1988) Reassessment of the scale-determining equation for advanced turbulence models. AIAA J 26:1299–1310. https://doi.org/10.2514/3.10041

Woolley RM, Fairweather M, Yunardi (2009) Conditional moment closure modelling of soot formation in turbulent, non-premixed methane and propane flames. Fuel 88:393–407. https://doi.org/10.1016/j.fuel.2008.10.005

Yamashita H (2000) Numerical study on NOx production of transitional fuel jet diffusion flame. JSME Int J Ser B 43:97–103. https://doi.org/10.1299/jsmeb.43.97

Yamashita H, Djamrak D, Takeno T (1999) Role of elementary reactions in flame structure and unsteady behavior of two-dimensional fuel jet diffusion flame. JSME Int J Ser B 42:699–707. https://doi.org/10.1299/jsmeb.42.699

Zeldovich YB (1946) The oxidation of nitrogen in combustion and explosions. Acta Physicochim URSS 21:577–628

Zettervall N, Fureby C, Nilsson EJK (2021) Evaluation of chemical kinetic mechanisms for methane combustion: a review from a CFD perspective. Fuels 2:210–240. https://doi.org/10.3390/fuels2020013